Shape optimization of porous structures by phase-field modeling with strain energy density reduction

Leonie Wallat [b,c,*], Martin Reder [a,c], Michael Selzer [d], Frank Poehler [b], Britta Nestler [c,d]

[a] Institute of Digital Materials Science, Karlsruhe University of Applied Sciences, Moltkestraße 30, 76133 Karlsruhe, Germany
[b] Institute of Materials and Processes, Karlsruhe University of Applied Sciences, Moltkestraße 30, 76133 Karlsruhe, Germany
[c] Institute for Applied Materials - Microstructure Modelling and Simulation, Karlsruhe Institute of Technology (KIT), Strasse am Forum 7, 76131 Karlsruhe, Germany
[d] Institute of Nanotechnology, Karlsruhe Institute of Technology (KIT), Hermann-von-Helmholtz-Platz 1, 76344 Eggenstein-Leopoldshafen, Germany

Keywords:
TPMS structures
Gyroid
Phase-field method
Shape optimization

A B S T R A C T

Triply periodic minimal surfaces (TPMS) are cell structures defined by mathematical formulas. Due to their special structure and properties, such as a high surface-to-volume ratio and good mechanical properties, these structures are used in a wide range of applications, *e.g.*, for implants or heat exchangers. Given the diverse applicability of these structures, both scientific and industrial interest resides in the tailored shape optimization, where structural integrity is preserved on the one hand, while stiffness is selectively enhanced on the other.

Therefore, in the following investigation, three TPMS unit cells are shape-optimized under mechanical loading, in the linear-elastic regime, by minimizing the strain energy density, using the phase-field method. The novelty lies in the shape optimization of TPMS structures with respect to the effective stiffness under mechanical load which is addressed with a phase-field method. It is shown that with the present optimization approach, an increase in the effective Young's modulus of up to 55% can be achieved for specific TPMS structures.

1. Introduction

Porouscell structures occurring in nature possess inherently beneficial and unique properties for their respective area of application. For example, they often exhibit a minimal surface as well as a low weight [1], which has made them interesting and promising for technical applications for decades. By developing additive manufacturing processes, it is possible to create structures with a complex geometry and controllable parameters such as porosity and cell size, *cf.*, *e.g.*, [2]. For instance, they can be produced from the Ti-6Al-4V alloy, utilizing the electron beam melting process [3,4]. In the study by Yan et al. [5], a novel approach combining 3D printing and material injection is presented. These advanced and established methodologies facilitate the fabrication of computationally designed complex structures and their practical utilization in real-world applications.

Triply-periodic minimal surfaces (TPMS) are an example of such complex structures [6,7]. TPMS structures are cell structures that are defined by mathematical formulas with controllable geometric parameters. Examples of such cell structures include sheet-based Schwarz diamond, gyroid and Schwarz primitive structures, as shown in Fig. 1(a)–(c).

The properties of these structures, such as a high surface-to-volume ratio and their periodicity, make them attractive for a wide range of applications. This involves research areas ranging from medical engineering [8–10] to electrochemical flow reactors [11]. Moreover, the mechanical properties of TPMS structures have already been investigated in several studies [12–16]. In [14], for example, gyroid structures are proposed as support structures, because of their robust and lightweight properties.

An optimal shape of these structures strongly depends on specific applications as well as on the considered property to be optimized. Thus, for particular physical processing conditions, a geometry optimization is desirable, where the TPMS structures can be used as the initial geometry for a shape optimization algorithm to further improve specific properties defined in a cost function. This can be achieved by employing methods of computer-based shape and topology optimization.

Such methods were developed and applied across a range of disciplines, driven by diverse physical properties to be optimized under different constraints. As a result, a multitude of optimization algorithms exists for various applications. An example are strategies developed

* Corresponding author at: Institute for Applied Materials - Microstructure Modelling and Simulation, Karlsruhe Institute of Technology (KIT), Strasse am Forum 7, 76131 Karlsruhe, Germany.

E-mail addresses: leonie.wallat@h-ka.de (L. Wallat), michael.selzer@kit.edu (M. Selzer), britta.nestler@kit.edu (B. Nestler).

and investigated in the field of fluid dynamics [17,18], in which *e.g.* the drag resistance is objected to optimization. In the context of solid mechanics, density-based filling algorithms have been extensively explored to improve the stiffness of porous structures [19]. Apart from this, shape optimization algorithms are also found in other fields like heat transport [20,21]. In order to achieve improvements with regard to different properties, TPMS structures have generally been used as the basis for various shape adjustments [22–24]. These works include approaches based on an automated optimization algorithm as well as manual shape adjustments. A porosity gradient, for example, was introduced into the structure, which, among other things, increases the surface-to-volume ratio, compared to structures with the same porosity [23]. Stromberg [24] introduces an automated multi-scale topology optimization method under mechanical loading, which generates combinations of macro layouts and locally graded TPMS-based lattice structures, with a specific emphasis on strut-based gyroid structures. This approach involves the introduction of two density fields in each finite element. Investigations into the optimization of TPMS structures for fluid mechanical applications have been conducted [20, 25]. In particular, these structures were optimized for enhanced heat dissipation, using a custom-designed methodology. The optimization process involves the development of a proprietary algorithm tailored to address the heat transfer requirements [20]. In [21], the triply periodic minimal surfaces are optimized with respect to thermal conductivity and stability.

The present work focuses on shape optimization, in the context of solid mechanics, with the aim of increasing the stiffness of TPMS structures. To our knowledge, such a mechanical application-specific shape optimization of these structures has not yet been undertaken. Therefore, a shape optimization algorithm based on the phase-field method is employed, where TPMS structures are used as initial geometry and optimized under mechanical loading. The advantages of phase field-based shape optimization lie in its capability to consider complex geometries without a geometry specific discretization like body fitted meshes. The phase-field method (PFM) enables the simulation of the temporal evolution of microstructures that are in a thermodynamically unstable state. It is widely in use for different fields of applications, including grain growth [26–28] and solidification [29]. In the field of solid mechanics, the phase-field method has been applied to model crack propagation [30–32], the phase transformation under mechanical driving forces such as martensitic phase transformation [33,34], as well as multigrain systems under load [35,36]. In the context of porous media, [37] uses the PFM to determine the effective stiffness of stochastic foams. Additionally, TPMS structures have been successfully generated and analyzed with the phase-field method. This demonstrates its versatility in various applications within the field of solid mechanics, involving multiple phases, which can also represent pores. In the publication [38], an algorithm was introduced to generate surfaces with constant mean curvature and simultaneous volume constraints, employing the phase-field method. This algorithm was exemplified through the generation of TPMS structures. In [39], the PFM was used to investigate TPMS structures with regard to flow characterization, in terms of permeability and inertial drag. Furthermore, a shape transformation was performed using the phase-field equation with a modified version of the Allen–Cahn equation [40]. However, a specific form optimization under mechanical loading was not addressed in this investigation.

Wang [41] also considers shape optimization in the field of mechanics, using a phase-field-type method. While the present work employs an Allen–Cahn approach, they apply the Van der Waals-Cahn–Hilliard approach and focus on 2D numerical examples. In [42], the Cahn–Hilliard approach is coupled with continuum mechanics for the optimization process, aiming to achieve an energetically optimized structure, which is demonstrated here using a beam structure as an example. For complex porous structures, such as TPMS structures, however, the utilization of a phase-field optimization approach has not been performed previously.

In the present study, a shape optimization is performed to reduce the total energy in the system and simultaneously increase the stiffness of three distinct single-cell TPMS structures – diamond, gyroid, and primitive – under mechanical loading. A vertical linear-elastic pressure load is considered as the loading condition. The shape optimization is performed using a modified phase-field equation, where the elastic energy is introduced as a driving force. Throughout the simulation, the volume is maintained constant, and in contrast to previous works, the periodicity of the structures in the x- and z-directions is preserved. This constant volume ensures a better comparability between the structures and prevents energy reduction in the system, through the addition of volume. For volume preserving optimization in the phase-field context, Cahn–Hilliard approaches are often employed. However, in the present work, we used the Allen–Cahn approach with a modification to achieve volume conservation. This approach is chosen, because the Allen–Cahn model requires less computational cost and is easier to solve, due to its second-order partial differential equation, whereas the Cahn–Hilliard models involve a fourth-order equation [43].

Maintaining periodicity in the x- and z-directions allows the optimized cell to be replicated multiple times in the respective spatial directions, making it suitable for applications such as sandwich components.

Overall, the structural optimization serves as an exemplary demonstration of load-oriented optimization for complex porous structures, using the phase-field method under mechanical loading. While shape optimization of TPMS structures was performed in other fields, an optimization with regard to their mechanical properties does not exist to the authors' knowledge. However, mechanical shape optimization has already been performed for other topologies, but not for TPMS structures. Thus, the novelty of the present work lies in the application of mechanical shape optimization to TPMS structures.

The presented computational approach facilitates a comprehensive understanding of the structural dynamics intrinsic to the phase-field optimization based on elastic energy.

The paper is structured as follows: The general formulation of the phase-field approach is presented in Section 2, followed by the introduction of the modified approach of the phase-field method. Based on the methodological framework, the focus in Section 3 is on applications of the modified phase-field method to optimize porous structures, with an emphasis on the TPMS structures.

2. Methodology of the shape optimization

The structure generation and the optimization procedure are based on the phase-field method and are implemented in the in-house software framework "Parallel Algorithms for Crystal Evolution in 3D" (Pace3D) [44]. This framework involves structural-mechanical simulations for a given loading scenario, in which the geometry is varied in such a way that the stored elastic energy is minimized. Subsequently, the algorithmic generation of TPMS structures, the phase-field modeling of the shape optimization, and the setup of the mechanical loading are described.

2.1. Structure generation and characterization

Different TPMS structures, such as sheet-based gyroid or primitive structures, can be modeled and created algorithmically. The special feature of the tool used is that the digital model allows a high flexibility with respect to morphological features. Thus, it is possible to individually adjust the porosity or a porosity distribution through the structure, as well as the domain size and cell repetitions of a period cell. The structures used for this study are a single-cell sheet-based Schwarz diamond structure (hereinafter referred to as diamond), a sheet-based gyroid structure (hereinafter referred to as gyroid), and a sheet-based Schwarz primitive structure (hereinafter referred to as primitive), with a uniform porosity of about 85%, see Fig. 1.

Fig. 1. Examples of TPMS unit cells: a. Diamond; b. Gyroid; c. Primitive.

Using the abbreviations $\tilde{x} = x/L_x$, $\tilde{y} = y/L_y$, and $\tilde{z} = z/L_z$ for the normalized coordinates, with respect to the unit cell lengths $\{L_x, L_y, L_z\}$, the formulas parametrizing the respective structures read [45]:

$$0 = \Big[\sin(2\pi\tilde{x})\sin(2\pi\tilde{y})\sin(2\pi\tilde{z}) + \sin(2\pi\tilde{x})\cos(2\pi\tilde{y})\cos(2\pi\tilde{z}) + \cos(2\pi\tilde{x})\sin(2\pi\tilde{y})\cos(2\pi\tilde{z}) + \cos(2\pi\tilde{x})\cos(2\pi\tilde{y})\sin(2\pi\tilde{z}) \Big]^2 - \delta^2 \tag{1}$$

$$0 = \Big[\sin(2\pi\tilde{x})\cos(2\pi\tilde{y}) + \sin(2\pi\tilde{y})\cos(2\pi\tilde{z}) + \cos(2\pi\tilde{x})\sin(2\pi\tilde{z}) \Big]^2 - \delta^2 \tag{2}$$

$$0 = \Big[\cos(2\pi\tilde{x}) + \cos(2\pi\tilde{y}) + \cos(2\pi\tilde{z}) \Big]^2 - \delta^2. \tag{3}$$

Here, the parameter δ controls the wall thickness of the structure [46]. In addition to the thickness parameter, the cell structure is characterized by the number of cell repetitions in the x-, y-, and z-direction and by the size of the unit cells $\{L_x, L_y, L_z\}$ [47].

2.2. Phase-field method

The structure optimization is performed on the basis of the phase-field method, which is an established tool for problems such as phase transformations [48,49] or structure mechanics in multigrain systems [33,50]. The geometry is parametrized by a field of phase variables $\phi_\alpha(\vec{x}, t)$ that indicate, whether the phase α occurs at a point $\vec{x}$ or not, which corresponds to a value of 1 or 0. Instead of a sharp interface between phases, a smooth transition region and thus a diffuse interface with a finite thickness is used, where ϕ_α takes values between 0 and 1. Hence, the phase variable ϕ_α can be interpreted as a local volume fraction of the phase α. This allows the use of interpolation schemes in the diffuse interface, and thus avoids the use of body-fitted meshes in the numerical solution process [29]. The evolution of the phase field is described with a volume-preserved Allen–Cahn approach [51], which is based on a Ginzburg–Landau free energy density functional [52]. Let N denote the number of phases and Ω denote the computational domain. Then, the energy density f of the free energy functional $\mathcal{F}$ depends on the phase-field tuple $\phi = \{\phi_1, \dots, \phi_N\}$ and the corresponding gradients, which in turn are functions of space and time $(\vec{x}, t)$. The functional takes the general form

$$\mathcal{F}(\phi) = \int_\Omega \epsilon\alpha(\phi, \nabla\phi) + \frac{1}{\epsilon}\omega(\phi) + f^{\mathrm{b}}(\phi)\, \mathrm{d}V. \tag{4}$$

Here, $\epsilon\alpha$ and $\frac{1}{\epsilon}\omega$ denote the gradient energy density and potential energy, which are nonzero only within the diffuse interface and represent the interfacial energy. How these terms can be modeled is described in [29], for example. The bulk energy of the phases is referred to as f^{b} and includes phase-inherent energies such as elastic energy density f^{el}, which can act as a driving force for phase transformation. In order to minimize the functional (4), variational calculus yields the condition

$$\forall \vec{x} \in \Omega, \alpha = 1, \dots, N: \quad \Psi_\alpha := \frac{\partial(\epsilon\alpha + \frac{1}{\epsilon}\omega + f^{\mathrm{b}})}{\partial\phi_\alpha} - \nabla \cdot \frac{\partial\epsilon\alpha}{\partial\nabla\phi_\alpha} = 0 \tag{5}$$

as a field equation inside the domain. Using the multiphase-field approach of Nestler et al. [29], a relaxation to the minimum yields the evolution equation

$$\frac{\partial\phi_\alpha}{\partial t} = \frac{1}{\tau\epsilon}\Psi_\alpha + \lambda \tag{6}$$

for each phase variable. Here, ϵ is a parameter that regulates the width of the diffuse interface, τ is a positive kinetic mobility coefficient, and λ is a Lagrange multiplier that ensures the summation constraint

$$\sum_{\alpha=1}^{N} \phi_\alpha = 1. \tag{7}$$

For details regarding the derivation of the evolution equation, we refer to the publication by Nestler et al. [29]. In the present publication, a phase system with $N = 2$ phases is assumed. The phase variable of the solid is denoted as ϕ_{s} and the pore phase is given by $1 - \phi_{\mathrm{s}}$, due to the summation constraint (7). In this special case, we have the dependencies $\frac{1}{\epsilon}\omega(\phi_{\mathrm{s}})$ and $\epsilon\alpha(\nabla\phi_{\mathrm{s}})$, and thus, the evolution of the solid phase is governed by

$$\frac{\partial\phi_{\mathrm{s}}}{\partial t} = \frac{1}{\tau\epsilon}\left[\frac{\partial(\frac{1}{\epsilon}\omega + f^{\mathrm{b}})}{\partial\phi_{\mathrm{s}}} - \nabla \cdot \frac{\partial\epsilon\alpha}{\partial\nabla\phi_{\mathrm{s}}}\right]. \tag{8}$$

In this work, the obstacle potential $\frac{1}{\epsilon}\omega = 16\gamma/(\pi^2\epsilon)\phi_{\mathrm{s}}(1 - \phi_{\mathrm{s}})$ is employed, which yields

$$\frac{\partial\phi_{\mathrm{s}}}{\partial t} = \frac{1}{\tau\epsilon}\left[2\gamma\epsilon\Delta\phi_{\mathrm{s}} - \frac{16\gamma}{\pi^2\epsilon}(1 - 2\phi_{\mathrm{s}}) + \frac{\partial f^{\mathrm{b}}}{\partial\phi_{\mathrm{s}}}\right], \tag{9}$$

where γ is the surface tension. This choice of potential results in a finite diffuse interface with a width of $\epsilon\pi^2/4$. The term resulting from the bulk energy density f^{b} is determined from the mechanical modeling introduced below.

2.3. Modified phase-field-method for shape optimization

The structural optimization aims to increase the effective stiffness, which corresponds to an elastic energy minimization. For this purpose, the phase-field equation is supplemented to a driving force, which results from differences in the elastic strain energy f^{el} of different phases. This driving force leads to a phase transformation and thus to a change in the shape of the initial geometry, which can be used to minimize the energy.

Subsequently, a hyper-elastic material behavior in the small deformation regime is considered, which yields the elastic free energy density

$$f^{\mathrm{el}}(\vec{u}) = \frac{1}{2}\boldsymbol{C}[\boldsymbol{\epsilon}] \cdot \boldsymbol{\epsilon}, \tag{10}$$

where $\boldsymbol{C}$ denotes the stiffness tensor, $\boldsymbol{\epsilon}$ the infinitesimal strain tensor, and $[\cdot]$ the linear mapping of second-order tensors, by a fourth-order tensor. The strain is given as the symmetric gradient of the displacement field $\vec{u}$, which is the solution variable for the solid mechanical problem. Furthermore, the stresses are related to the strains via Hooke's law [53]

$$\boldsymbol{\sigma} = \frac{\partial f^{\mathrm{el}}}{\partial\boldsymbol{\epsilon}} = \boldsymbol{C}[\boldsymbol{\epsilon}]. \tag{11}$$

In the context of the phase-field method, the effective values for strains and stresses must be calculated from the phase-inherent values within the diffuse interface [54]. Here, we use the approach of Khachaturian [55], which uses an interpolated stiffness tensor and assumes that the phase-inherent strains in the interface are identical at each

interfacial point. In this approach, the stress and strain fields represent common effective quantities of the mixture in the diffuse interface and therefore need not be distinguished between different phases. Since the pore phase does not exhibit any stiffness, the Khachaturian interpolation approach yields the interpolated stiffness $\boldsymbol{C} = h(\phi_s)\boldsymbol{C}_s$ and the relations

$$\boldsymbol{\sigma} = h(\phi_s)\boldsymbol{C}_s[\boldsymbol{\epsilon}], \tag{12}$$

$$f^{el} = \frac{1}{2}h(\phi_s)\boldsymbol{C}_s[\boldsymbol{\epsilon}] \cdot \boldsymbol{\epsilon}, \tag{13}$$

where $h(\phi_s)$ is an interpolation function and $\boldsymbol{C}_s$ denotes the stiffness tensor of the solid phase. The interpolation function needs to satisfy the conditions $h(0) = 0$, $h(1) = 1$, and the summation constraint $\sum_\alpha h(\phi_\alpha) = 1$. Under these restrictions, different choices for the interpolation function are possible, which essentially regulates the steepness of the interpolation between material parameters. For more details, we refer to the publications [56,57]. In the present paper, the interpolation function is used to interpolate the phase-inherent stiffness tensors with the expression $h(\phi_s) = \phi_s^3(10 - 15\phi_s + 6\phi_s^2)$. The elastic free energy density contributes to the bulk energy term f^b of the free energy functional. Therefore, in addition to the phase evolution, the momentum balance

$$\nabla \cdot (\boldsymbol{\sigma}) = 0 \tag{14}$$

is also obtained from the free energy functional (4), using the variational procedure. This leads to a coupled problem consisting of phase evolution equations and the steady-state momentum balance.

During shape optimization, a constant volume of the solid phase is aimed for. Since the Allen–Cahn approach by itself is not volume preserving, an additional energy contribution $g(\phi_s)$ is necessary, which ensures volume conservation [58]. This results in a Lagrange multiplier entering the Allen–Cahn equation, which enforces $\frac{d}{dt}\int_\Omega \phi_s \, dV = 0$. Therefore, the bulk energy density in the functional (4) reads:

$$f^b(\phi_s, \vec{u}) = g(\phi_s) + w f^{el}(\vec{u}). \tag{15}$$

Here, the elastic energy is scaled by the weighting parameter w. This parameter controls the strength of the mechanical driving forces, and thus, how fast the shape of the structure changes during the optimization process. The consideration of a physical process would require $w = 1$, so as to capture the dynamics correctly. However, in this work, the phase transformation does not model a physical process, but is part of an optimization algorithm searching for geometries that minimize the cost function, which is the elastic free energy of the system. Therefore, w can be chosen freely and it represents a relaxation parameter of the optimization algorithm.

Substituting the bulk energy density (15) into the phase-field evolution equation (9) yields

$$\frac{\partial \phi_s}{\partial t} = \frac{1}{\tau\epsilon}\left[2\gamma\epsilon\Delta\phi_s - \frac{16\gamma}{\pi^2\epsilon}(1 - 2\phi_s) + \frac{\partial g}{\partial \phi_s} + \frac{\partial h}{\partial \phi_s}\frac{1}{2}\boldsymbol{C}_s[\boldsymbol{\epsilon}] \cdot \boldsymbol{\epsilon}\right]. \tag{16}$$

For the detailed form of g, we refer to [58]. This evolution equation describes a volume-preserving phase transformation that iteratively changes the geometry toward the minimum free energy. Again, it has to be pointed out that this phase transformation does not represent a physical process, but the search for an optimal shape. Thus, t represents a pseudo-time and the mobility parameter τ as well as the weighting parameter w are purely numerical parameters which determine the speed of the geometry variation. This also holds for the surface tension γ. In the present case, it weights the interface terms compared to the bulk terms. The surface tension for the current optimization process is to be chosen high enough to preserve the phase-field equilibrium profile over time. It should also be small enough not to introduce a high amount of curvature minimization dynamics. The ratio of surface tension forces and elastic forces is characterized by the dimensionless number $\gamma/(LEw)$, where L is the domain length and E the Young's modulus of the material. Here, a value of 5.7×10^{-6} is used, which indicates that the phase evolution is mainly driven by elasticity and the surface-minimizing dynamics of the phase-field evolution is negligible.

2.4. Optimization procedure and choice of parameters

For the present optimization procedure, the cost function is the total free energy

$$\mathcal{F} = \int_\Omega \gamma\left(\epsilon\nabla\phi_s \cdot \nabla\phi_s + \frac{16}{\pi^2\epsilon}\phi_s(1 - \phi_s)\right) + g(\phi_s) + \frac{1}{2}h(\phi_s)\boldsymbol{C}_s[\boldsymbol{\epsilon}] \cdot \boldsymbol{\epsilon} \, dV \tag{17}$$

of the system, which is minimized under the constraint of preserved volume. The solid phase variable ϕ_s serves as a design variable representing the structural geometry. Therefore, the optimization problem can be stated as

$$\min\big(\mathcal{F}(\phi_s)\big) \quad \text{under} \quad \int_\Omega \phi_s \, dV = V_s, \tag{18}$$

where V_s is the initial volume of the solid phase. We are also interested in finding an optimum that preserves the topology of the initial TPMS structure, which acts as another constraint. As mentioned earlier, the surface tension γ is chosen to be very small and the total free energy $\mathcal{F}$ is driven almost solely by its elastic contribution. Thus, the minimization of $\mathcal{F}$ is roughly equivalent to the minimization of the total elastic energy of the system, which results in a maximum effective stiffness under the given mechanical boundary conditions. To arrive at a minimization of the free energy, the equation system containing the phase-field evolution equation (16), coupled with the stationary momentum balance (14), is considered, which yields

$$\nabla \cdot (\boldsymbol{\sigma}) = 0, \qquad \boldsymbol{\sigma} = h(\phi_s)\boldsymbol{C}_s[\boldsymbol{\epsilon}], \tag{19}$$

$$\frac{\partial \phi_s}{\partial t} = \frac{1}{\tau\epsilon}\left[2\gamma\epsilon\Delta\phi_s - \frac{16\gamma}{\pi^2\epsilon}(1 - 2\phi_s) + \frac{\partial g(\phi_s)}{\partial \phi_s} + \frac{\partial h(\phi_s)}{\partial \phi_s}\frac{1}{2}\boldsymbol{C}_s[\boldsymbol{\epsilon}] \cdot \boldsymbol{\epsilon}\right]. \tag{20}$$

For the numerical solution of the system of equations, a Cartesian grid is chosen for spatial discretization. For the phase-field equation, a finite-difference method with explicit time integration is employed. In each time step, the momentum balance is solved up to equilibrium, using a finite element discretization with linear elements. The resulting linear system of the momentum balance is solved with a conjugate gradient method. Further details of the solution procedure can be found in [59], where a similar approach is used to couple elasticity and phase evolution. The optimization algorithm is stopped as soon as a further phase evolution would introduce topological changes.

The shape optimization performed in the further course is done using $\epsilon = 0.015L$, which corresponds to an interface width of approximately $0.0375L$, where the edge length $L = 2.5\,\text{mm}$ of the domain is considered. This choice ensures a resolution of the diffuse interface with a number of 7 cells. Furthermore, we choose $\gamma = 21\,\text{kg}\,\text{s}^{-2}$, the mobility parameter $\tau = 1.0\,\text{kg}\,\text{s}^{-1}\,\text{m}^{-1}$, a weighting of the driving forces of $w = 0.025$. The time step size is $\Delta t = 7.46 \times 10^{-14}\,\text{s}$. In the following process, a total of 50 time steps are taken into account, which corresponds to a frame step. We examine the different stages of development during the optimization of TPMS structures. Intermediate results provide insights into the underlying mechanisms and transformations that occur during the optimization of TPMS structures. The simulation is interrupted when the topology begins to change, which is attributed to the displacement of the interface. Otherwise, the structure would emerge into a lamellar-shaped component as stationary solution of the phase-field evolution equation under the given mechanical boundary conditions.

2.5. Setup for mechanical simulations

The shape of the initial structure is energetically optimized under unilateral compressive loading, as shown in Fig. 2. The resulting optimized cells can then be used for further investigations and applications, for example as cores in sandwich components [60].

A pseudo-time records the process in which the structure geometry changes successively toward the optimal shape. According to Eq. (14), a stationary structure-mechanical solution is calculated for each time

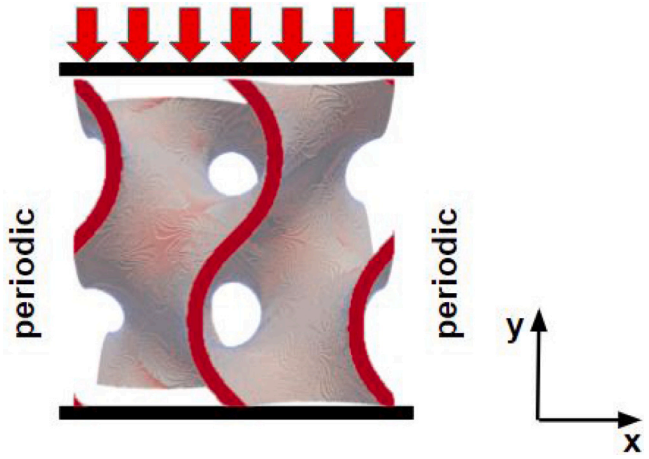

Fig. 2. Boundary conditions of the initial structure.

step. Subsequently, 200 × 200 × 200 grid cells are initialized for three-dimensional microstructure simulations, while the two-dimensional examples are discretized with 200 × 200 cells. Isotropically elastic behavior is assumed for the structural material, while the pore phase is modeled with a residual stiffness of one thousandth of the solid material.

The load on the structure is applied in the y-direction, with a constant stress of 400 MPa, while periodic boundary conditions are assumed in both x- and z-directions. The TPMS structure is considered to consist of an isotropic material with a mass density of 2680 kg mm^{-3}, a Young's modulus of 59 GPa, and the Poisson ratio 0.35. In addition, a homogenization is performed, in which the effective stiffness of the structure is determined from the stress and strain field [61,62]. If the effective stress is constant, as is the case in this work, structures that minimize the elastic free energy yield a maximum effective stiffness. A homogenization approach allows the transfer of results from the micro to the macro level *cf.*, *e.g.*, [37]. The following mechanical analysis values, such as the effective Young's modulus, are accordingly given in dimensionless values. As the publication by Wallat et al. [12] has already shown, the sequence of values corresponds to that of experimental data.

3. Results and discussion

3.1. Data-driven structure linkages

The computational optimization is based on the phase-field method, which reduces the total energy density in the system by shifting the interface to the energetically more favorable region. Consequently, the initially considered structures evolve over time into structures with a new topology. The optimized structure no longer resembles the initial structures. Since we are interested in TPMS-like structures, the simulation is terminated as soon as the topology of the initial structure is changed. Fig. 3 shows the shape-optimized structures of the last simulation step, frame 10. As described in detail in Section 2.3, one frame step corresponds to fifty time steps.

When looking at the shape-optimized structures, it becomes evident that a volume redistribution has taken place during the shape optimization. As can be seen from the diagrams 4–6, volume was added to highly energetic (and correspondingly loaded) areas, while volume was subtracted from less stressed areas, resulting in energy minimization in the overall system. The energy is plotted on the primary x-axis, while the volume fraction is plotted on the secondary x-axis, across the layers. The initial structure is shown with a dotted line, while the optimized structure is shown with a solid line. From the volume distribution of the initial structure, the characteristic periodic shape, which progresses in the y-direction, can be seen for all three structures. After shape optimization, the volume fraction of the uppermost layers is increased for all three structures in the y-direction, while it is removed from less energetic regions. The temporal energy reduction, which takes place for all three structures, is shown comparatively in the bar chart 7.

The diagram shows that after each simulation step, the energy in the system is reduced. The primitive structure has the highest initial energy, followed by the gyroid structure. The diamond structure has the lowest energy. In the case of the diamond structure, shape optimization reduces the energy in the overall system by about 38%, while for the gyroid structure, the energy is reduced by about 34% and for the primitive structure by about 13%. As a result, the diamond structure has the highest energetic reduction in the overall system.

Table 1 compares the development of the volume fraction, the surface-to-volume ratio, and the effective Young's modulus during the shape optimization process of all three structures. Frame 0 represents the initial structure. Since the surface-to-volume ratio is important in engineering applications, such as heat exchangers [63], this property was selected.

The volume fraction, which is about 85% in porosity for all structures, is kept constant during shape optimization. Between the structures, a porosity variation of about 4% can be observed.

Comparing the energy with the effective modulus of elasticity in Table 1, the structure with the highest energy has the lowest effective Young's modulus and vice versa. Accordingly, the diamond cell has the highest effective Young's modulus and the primitive cell the lowest. In general, the effective Young's modulus could be increased from 20% (primitive) to 55% (diamond). The ranking of the Young's modulus of the initial structures can be confirmed by various studies [15,64]. In the publication by Naghavi et al. [15], for example, the mechanical properties of gyroid and diamond structures of Ti6Al4V were compared for later use as bone implants. It was discussed that the diamond structure also has a higher Young's modulus than the gyroid structure. This order is maintained during shape optimization.

In general, the diamond cell has the highest surface-to-volume ratio, followed by the gyroid structure and the primitive structure. For both the diamond structure and the primitive structure, no reduction in the surface-to-volume ratio was observed during the shape optimization process. For the primitive structure, a slight increase from 0.164 to 0.167 was observed. At the beginning of the shape optimization process, the gyroid structure results in a slight decrease in the surface-to-volume ratio. From frame 9, however, a slight increase from 0.211 to 0.213 can be observed.

As a consequence, the TPMS structures lose their property of periodicity in all spatial directions. Due to the previously mentioned "periodic" boundary condition in the x- and z-directions, the periodicity in these directions could be preserved. This means that a later multiplication in the respective spatial directions and a later adaptation to the geometry would be possible for later applications.

4. Conclusion

In this work, a shape optimization based on the phase-field method is performed on TPMS structures. It is shown that while maintaining the topology of the respective TPMS structures, their structure could be shape-optimized by minimizing the energy in the system, using the phase-field method. Overall, an increase of the effective Young's modulus could be achieved by the interfacial displacement, with the same volume and a simultaneous partial increase in the surface-to-volume ratio. For all three structures, the effective Young's modulus was increased by at least 20%. The largest improvement is found for the diamond structure, which showed an increase of 55%.

The characteristic property of the TPMS unit cell, which is periodic in all spatial directions, is no longer preserved after the shape optimization. This periodicity could only be maintained in the x- and

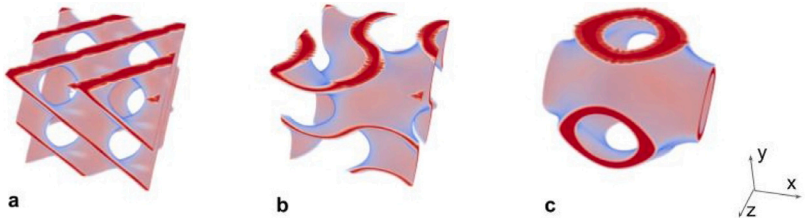

Fig. 3. Shape-optimized structures - a. Diamond; b. Gyroid; c. Primitive.

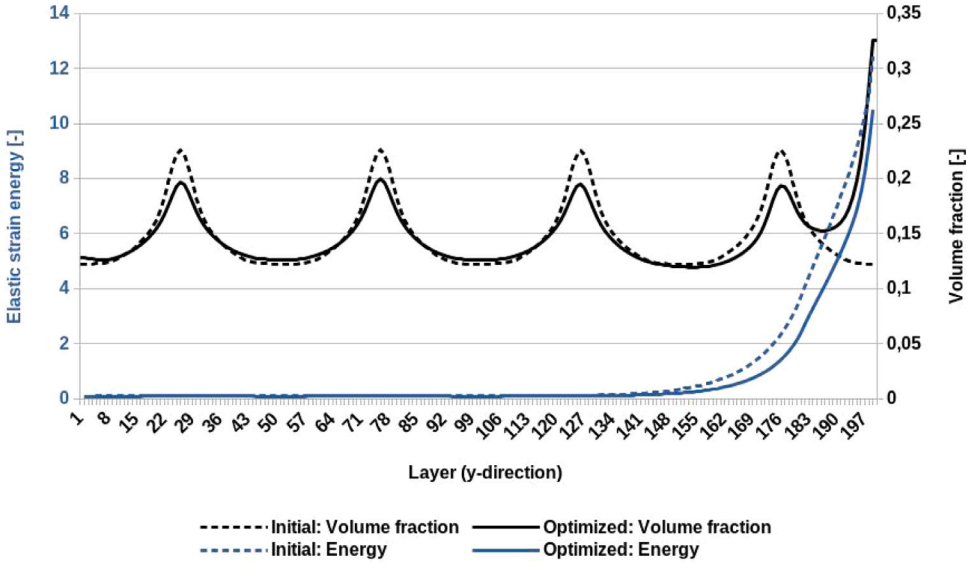

Fig. 4. Energy (primary axis) and volume (secondary axis) distribution of the diamond structure in the *y*-direction of the initial structure (dashed line) and the optimized structure (solid line), as well as the volume difference of the two structures.

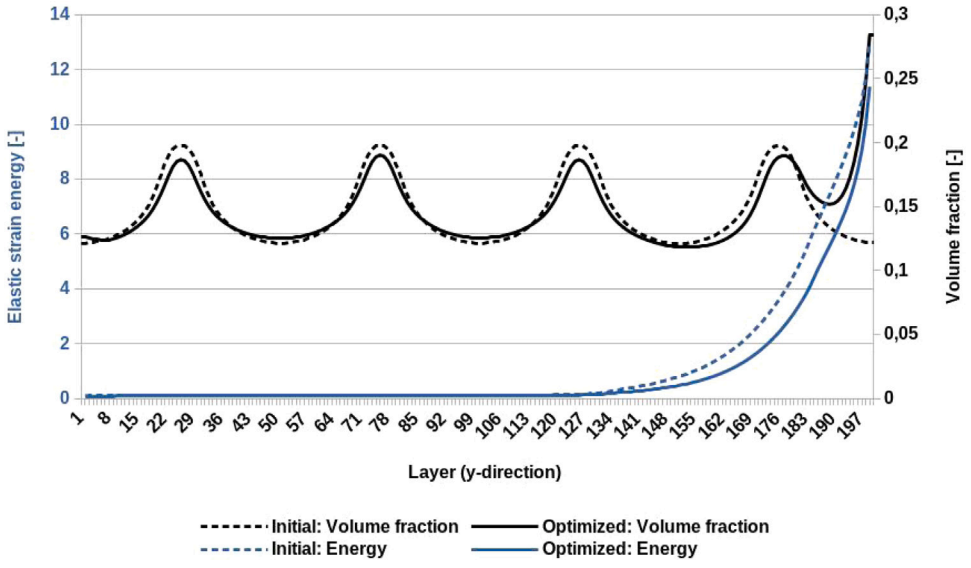

Fig. 5. Energy (primary axis) and volume (secondary axis) distribution of the gyroid structure in the *y*-direction of the initial structure (dashed line) and the optimized structure (solid line), as well as the volume difference of the two structures.

z-directions. However, by preserving the shape, other characteristics such as the high surface-to-volume ratio, which is of interest for certain engineering applications, could be retained. The influence of structural properties, such as the surface-to-volume ratio and the boundary conditions, on the effective Young's modulus was not investigated in this work. Therefore, the influence of the boundary conditions on the mechanical properties can be addressed in future investigations.

In general, these results open up new design possibilities, especially in areas where stability and low weight are required. The structures for sandwich cores, whose periodicity could be maintained in the

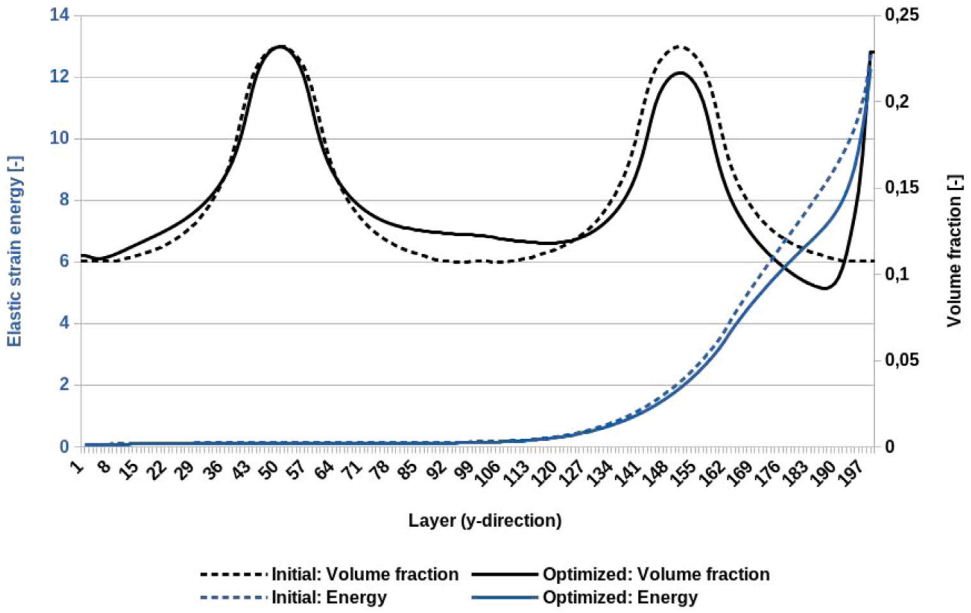

Fig. 6. Energy (primary axis) and volume (secondary axis) distribution of the primitive structure in the *y*-direction of the initial structure (dashed line) and the optimized structure (solid line), as well as the volume difference of the two structures.

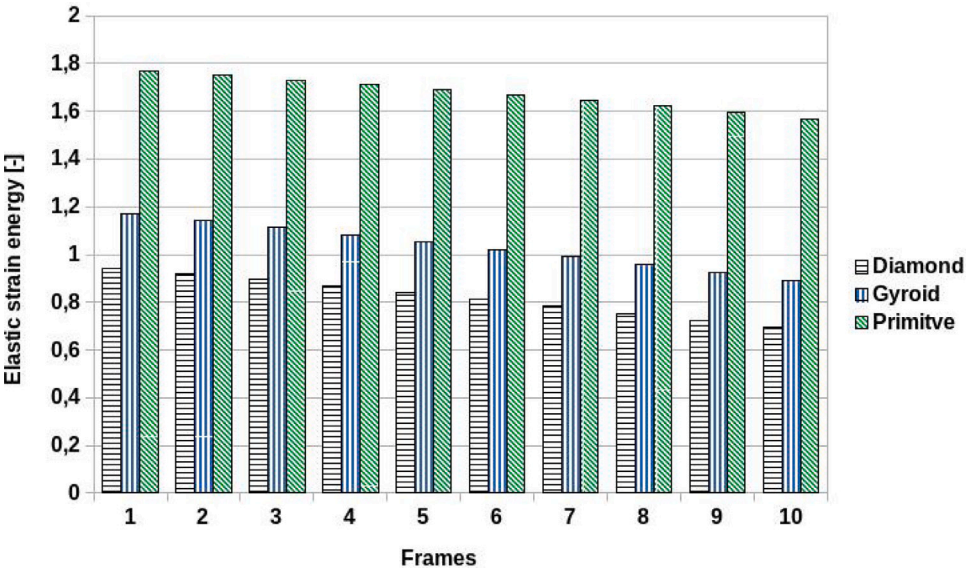

Fig. 7. Course of the decrease of the internal energy of the shape-optimized TPMS.

Table 1
Development of the structural and mechanical properties of the initial structures (frame 0), up to the shape-optimized structure (frame 10).

Frame	Diamond			Gyroid			Primitive		
	Volume fraction	Surface/ volume ratio	Young's modulus (dim.less)	Volume fraction	Surface/ volume ratio	Young's modulus (dim.less)	Volume fraction	Surface/ volume ratio	Young's modulus (dim.less)
0	**0.148**	**0.258**	**2.186**	**0.146**	**0.211**	**1.748**	**0.143**	**0.164**	**0.989**
1	0.148	0.258	2.244	0.146	0.210	1.800	0.143	0.164	1.005
2	0.148	0.258	2.321	0.146	0.210	1.853	0.143	0.164	1.022
3	0.148	0.258	2.403	0.146	0.211	1.909	0.143	0.165	1.029
4	0.148	0.258	2.493	0.146	0.211	1.970	0.143	0.166	1.057
5	0.148	0.258	2.594	0.146	0.211	2.034	0.143	0.166	1.077
6	0.148	0.258	2.706	0.146	0.211	2.104	0.143	0.166	1.097
7	0.148	0.258	2.954	0.146	0.212	2.180	0.143	0.166	1.118
8	0.148	0.258	3.091	0.146	0.212	2.262	0.143	0.166	1.141
9	0.148	0.258	3.240	0.146	0.213	2.350	0.143	0.166	1.165
10	0.148	0.258	3.403	0.146	0.213	2.444	0.143	0.167	1.190

x- and z-direction, and the fact that an arbitrary duplication of the optimized structures in the respective spatial directions is possible, are very interesting for further research. In addition, lookup tables can be created that contain optimized structures for various process treatments.

The next step would therefore be to study the structures experimentally. In the simulative area, extensions of the approach to perform topology optimization in addition to shape optimization are the objective of future research.

CRediT authorship contribution statement

Leonie Wallat: Conceptualization, Methodology, Writing – original draft. **Martin Reder:** Writing – review & editing. **Michael Selzer:** Supervision, Project administration. **Frank Poehler:** Supervision, Project administration, Funding acquisition. **Britta Nestler:** Supervision, Project administration, Funding acquisition.

Declaration of competing interest

The authors declare that they have no known competing financial interests or personal relationships that could have appeared to influence the work reported in this paper.

Data availability

Data will be made available on request.

Acknowledgments

The authors would like to thank Leon Geisen for his editorial support and Andreas Reiter for his professional support. Thanks also go to the German Federal Ministry of Economics and Climate Protection, which is funding the ZIM project KK5134113SK1. The model development was supported by the program “MSE”, No. 43.31.01, funded by the Helmholtz Association.

References

[1] L.J. Gibson, Cellular solids, Mrs Bull. 28 (4) (2003) 270–274.

[2] O. Al-Ketan, R. Rowshan, R.K.A. Al-Rub, Topology-mechanical property relationship of 3D printed strut, skeletal, and sheet based periodic metallic cellular materials, Addit. Manuf. 19 (2018) 167–183, http://dx.doi.org/10.1016/j.addma.2017.12.006.

[3] S. Evsevleev, T. Mishurova, D. Khrapov, A. Paveleva, D. Meinel, R. Surmenev, M. Surmeneva, A. Koptyug, G. Bruno, X-ray computed tomography procedures to quantitatively characterize the morphological features of triply periodic minimal surface structures, Materials 14 (11) (2021) http://dx.doi.org/10.3390/ma14113002, URL https://www.mdpi.com/1996-1944/14/11/3002.

[4] D. Khrapov, M. Kozadayeva, K. Manabaev, A. Panin, W. Sjöström, A. Koptyug, T. Mishurova, S. Evsevleev, D. Meinel, G. Bruno, D. Cheneler, R. Surmenev, M. Surmeneva, Different approaches for manufacturing Ti-6Al-4V alloy with triply periodic minimal surface sheet-based structures by electron beam melting, Materials 14 (17) (2021) http://dx.doi.org/10.3390/ma14174912, URL https://www.mdpi.com/1996-1944/14/17/4912.

[5] X. Yan, C. Rao, L. Lu, A. Sharf, H. Zhao, B. Chen, Strong 3D printing by TPMS injection, IEEE Trans. Vis. Comput. Graphics 26 (10) (2020) 3037–3050, http://dx.doi.org/10.1109/TVCG.2019.2914044.

[6] S. Yu, J. Sun, J. Bai, Investigation of functionally graded TPMS structures fabricated by additive manufacturing, Mater. Des. 182 (2019) 108021, http://dx.doi.org/10.1016/j.matdes.2019.108021, URL https://www.sciencedirect.com/science/article/pii/S0264127519304599.

[7] C. Yan, L. Hao, A. Hussein, P. Young, Ti–6Al–4V triply periodic minimal surface structures for bone implants fabricated via selective laser melting, J. Mech. Behav. Biomed. Mater. 51 (2015) 61–73, http://dx.doi.org/10.1016/j.jmbbm.2015.06.024, URL https://www.sciencedirect.com/science/article/pii/S1751616115002295.

[8] Z. Dong, X. Zhao, Application of TPMS structure in bone regeneration, Eng. Regen. 2 (2021) 154–162, http://dx.doi.org/10.1016/j.engreg.2021.09.004, URL https://www.sciencedirect.com/science/article/pii/S2666138121000128.

[9] J. Feng, J. Fu, C. Shang, Z. Lin, B. Li, Porous scaffold design by solid T-splines and triply periodic minimal surfaces, Comput. Methods Appl. Mech. Engrg. 336 (2018) 333–352, http://dx.doi.org/10.1016/j.cma.2018.03.007, URL https://www.sciencedirect.com/science/article/pii/S0045782518301245.

[10] N.S.A. Hashimi, S.S. Soman, M. Govindharaj, S. Vijayavenkataraman, 3D printing of complex architected metamaterial structures by simple material extrusion for bone tissue engineering, Mater. Today Commun. 31 (2022) 103382, http://dx.doi.org/10.1016/j.mtcomm.2022.103382, URL https://www.sciencedirect.com/science/article/pii/S2352492822002525.

[11] F. Wiesner, A. Limper, C. Marth, A. Brodersen, M. Wessling, J. Linkhorst, Additive manufacturing of intertwined electrode pairs - Guided mass transport with gyroids, Adv. Eng. Mater. n/a (n/a) (2022) 2200986, http://dx.doi.org/10.1002/adem.202200986, arXiv:https://onlinelibrary.wiley.com/doi/pdf/10.1002/adem.202200986. URL https://onlinelibrary.wiley.com/doi/abs/10.1002/adem.202200986.

[12] L. Wallat, M. Selzer, U. Wasmuth, F. Poehler, B. Nestler, Energy absorption capability of graded and non-graded sheet-based gyroid structures fabricated by microcast processing, J. Mater. Res. Technol. 21 (2022) 1798–1810, http://dx.doi.org/10.1016/j.jmrt.2022.09.093, URL https://www.sciencedirect.com/science/article/pii/S2238785422015009.

[13] I. Maskery, N. Aboulkhair, A. Aremu, C. Tuck, I. Ashcroft, Compressive failure modes and energy absorption in additively manufactured double gyroid lattices, Addit. Manuf. 16 (2017) 24–29, http://dx.doi.org/10.1016/j.addma.2017.04.003, URL https://www.sciencedirect.com/science/article/pii/S2214860417301203.

[14] M. Pelanconi, A. Ortona, Nature-inspired, ultra-lightweight structures with gyroid cores produced by additive manufacturing and reinforced by unidirectional carbon fiber ribs, Materials 12 (24) (2019) http://dx.doi.org/10.3390/ma12244134, URL https://www.mdpi.com/1996-1944/12/24/4134.

[15] S.A. Naghavi, M. Tamaddon, A. Marghoub, K. Wang, B.B. Babamiri, K. Hazeli, W. Xu, X. Lu, C. Sun, L. Wang, M. Moazen, L. Wang, D. Li, C. Liu, Mechanical characterisation and numerical modelling of TPMS-based gyroid and diamond Ti6Al4V scaffolds for bone implants: An integrated approach for translational consideration, Bioengineering 9 (10) (2022) http://dx.doi.org/10.3390/bioengineering9100504, URL https://www.mdpi.com/2306-5354/9/10/504.

[16] H. Zhou, N. He, D.Z. Zhang, M. Zhao, T. Zhang, X. Ma, Mechanical properties of functionally graded rotating lattice structures fabricated with SLM process, Mater. Today Commun. 33 (2022) 104740, http://dx.doi.org/10.1016/j.mtcomm.2022.104740, URL https://www.sciencedirect.com/science/article/pii/S2352492822015811.

[17] B. Mohammadi, O. Pironneau, Shape optimization in fluid mechanics, Annu. Rev. Fluid Mech. 36 (1) (2004) 255–279, http://dx.doi.org/10.1146/annurev.fluid.36.050802.121926.

[18] C. Dapogny, P. Frey, F. Omnès, Y. Privat, Geometrical shape optimization in fluid mechanics using FreeFem++, Struct. Multidiscip. Optim. 58 (2018) http://dx.doi.org/10.1007/s00158-018-2023-2.

[19] J.P. Groen, J. Wu, O. Sigmund, Homogenization-based stiffness optimization and projection of 2D coated structures with orthotropic infill, Comput. Methods Appl. Mech. Engrg. 349 (2019) 722–742, http://dx.doi.org/10.1016/j.cma.2019.02.031, URL https://www.sciencedirect.com/science/article/pii/S0045782519301021.

[20] S. Wang, Y. Jiang, J. Hu, X. Fan, Z. Luo, Y. Liu, L. Liu, Efficient representation and optimization of TPMS-based porous structures for 3D heat dissipation, Comput. Aided Des. 142 (2022) 103123, http://dx.doi.org/10.1016/j.cad.2021.103123, URL https://www.sciencedirect.com/science/article/pii/S0010448521001342.

[21] D. Li, N. Dai, Y. Tang, G. Dong, Y.F. Zhao, Design and optimization of graded cellular structures with triply periodic level surface-based topological shapes, J. Mech. Des. 141 (7) (2019) http://dx.doi.org/10.1115/1.4042617, 071402. arXiv:https://asmedigitalcollection.asme.org/mechanicaldesign/article-pdf/141/7/071402/6419111/md_141_7_071402.pdf.

[22] Y. Jung, K. Chu, S. Torquato, A variational level set approach for surface area minimization of triply-periodic surfaces, J. Comput. Phys. 223 (2) (2007) 711–730, http://dx.doi.org/10.1016/j.jcp.2006.10.007, URL https://www.sciencedirect.com/science/article/pii/S0021999106004700.

[23] L. Wallat, P. Altschuh, M. Reder, B. Nestler, F. Poehler, Computational design and characterisation of gyroid structures with different gradient functions for porosity adjustment, Materials 15 (10) (2022) http://dx.doi.org/10.3390/ma15103730, URL https://www.mdpi.com/1996-1944/15/10/3730.

[24] N. Strömberg, A new multi-scale topology optimization framework for optimal combinations of macro-layouts and local gradings of TPMS-based lattice structures, Mech. Based Des. Struct. Mach. (2022) 1–18, http://dx.doi.org/10.1080/15397734.2022.2107538.

[25] Y. Jiang, J. Hu, S. Wang, N. Lei, Z. Luo, L. Liu, Meshless optimization of triply periodic minimal surface based two-fluid heat exchanger, Comput. Aided Des. 162 (2023) 103554, http://dx.doi.org/10.1016/j.cad.2023.103554, URL https://www.sciencedirect.com/science/article/pii/S0010448523000866.

[26] I. Steinbach, Phase-Field Models in Materials Science. Vol. 17. No. 7, 2009, http://dx.doi.org/10.1088/0965-0393/17/7/073001, 073001.

[27] N. Moelans, B. Blanpain, P. Wollants, An introduction to phase-field modeling of microstructure evolution, CALPHAD 32 (2) (2008) 268–294, http://dx.doi.org/10.1016/j.calphad.2007.11.003, URL https://www.sciencedirect.com/science/article/pii/S0364591607000880.

[28] Y. Wu, Q. Luo, E. wei Qin, Influencing factors of abnormal grain growth in Mg alloy by phase field method, Mater. Today Commun. 22 (2020) 100790, http://dx.doi.org/10.1016/j.mtcomm.2019.100790, URL https://www.sciencedirect.com/science/article/pii/S2352492819306531.

[29] B. Nestler, H. Garcke, B. Stinner, Multicomponent alloy solidification: Phase-field modeling and simulations, Phys. Rev. E Stat. Nonlinear Soft Matter Phys. 71 (2005) 041609, http://dx.doi.org/10.1103/PhysRevE.71.041609.

[30] M. Ambati, T. Gerasimov, L. De Lorenzis, A review on phase-field models of brittle fracture and a new fast hybrid formulation, Comput. Mech. 55 (2) (2015) 383–405.

[31] L. Schöller, D. Schneider, C. Herrmann, A. Prahs, B. Nestler, Phase-field modeling of crack propagation in heterogeneous materials with multiple crack order parameters, Comput. Methods Appl. Mech. Engrg. 395 (2022) 114965.

[32] Y. Li, T. Yu, C. Xing, S. Natarajan, Crack growth in homogeneous media using an adaptive isogeometric fourth-order phase-field model, Comput. Methods Appl. Mech. Engrg. 413 (2023) 116122, http://dx.doi.org/10.1016/j.cma.2023.116122, URL https://www.sciencedirect.com/science/article/pii/S0045782523002463.

[33] E. Schoof, D. Schneider, N. Streichhan, T. Mittnacht, M. Selzer, B. Nestler, Multiphase-field modeling of martensitic phase transformation in a dual-phase microstructure, Int. J. Solids Struct. 134 (2018) 181–194, http://dx.doi.org/10.1016/j.ijsolstr.2017.10.032.

[34] M. Javanbakht, M. Ghaedi, Interaction of martensitic transformations and vacancy diffusion at the nanoscale under thermal loading: A phase field model and simulations, Acta Mech. 232 (2021) http://dx.doi.org/10.1007/s00707-021-03067-5.

[35] T.Q. Bui, X. Hu, A review of phase-field models, fundamentals and their applications to composite laminates, Eng. Fract. Mech. 248 (2021) 107705, http://dx.doi.org/10.1016/j.engfracmech.2021.107705, URL https://www.sciencedirect.com/science/article/pii/S0013794421001582.

[36] S. Daubner, M. Reder, N. Prajapati, D. Schneider, B. Nestler, Multiphase-field modelling of anisotropic elasticity at finite deformation in Eulerian space, J. Comput. Sci. 66 (2023) 101930, http://dx.doi.org/10.1016/j.jocs.2022.101930, URL https://www.sciencedirect.com/science/article/pii/S1877750322002897.

[37] M. Reder, J. Holland-Cunz, P. Lorson, A. August, B. Nestler, Simulative determination of effective mechanical properties for digitally generated foam geometries, Adv. Eng. Mater. n/a (n/a) (2023) 2300340, http://dx.doi.org/10.1002/adem.202300340, arXiv:https://onlinelibrary.wiley.com/doi/pdf/10.1002/adem.202300340. URL https://onlinelibrary.wiley.com/doi/abs/10.1002/adem.202300340.

[38] S.-D. Yang, H.G. Lee, J. Kim, A phase-field approach for minimizing the area of triply periodic surfaces with volume constraint, Comput. Phys. Comm. 181 (6) (2010) 1037–1046, http://dx.doi.org/10.1016/j.cpc.2010.02.010, URL https://www.sciencedirect.com/science/article/pii/S0010465510000494.

[39] S. Rathore, B. Mehta, P. Kumar, M. Asfer, Flow characterization in triply-periodic-minimal-surface (TPMS) based porous geometries: Part 1 - hydrodynamics, Transp. Porous Media 146 (2022) http://dx.doi.org/10.1007/s11242-022-01880-7.

[40] H. Kim, C. Lee, S. Yoon, Y. Choi, J. Kim, A fast shape transformation using a phase-field model, Extreme Mech. Lett. 52 (2022) 101633, http://dx.doi.org/10.1016/j.eml.2022.101633, URL https://www.sciencedirect.com/science/article/pii/S2352431622000190.

[41] M. Wang, S. Zhou, Synthesis of shape and topology of multi-material structures with a phase-field method, J. Comput.-Aided Mater. Des. 11 (2004) 117–138, http://dx.doi.org/10.1007/s10820-005-3169-y.

[42] A. Bartels, P. Kurzeja, J. Mosler, Cahn–Hilliard phase field theory coupled to mechanics: Fundamentals, numerical implementation and application to topology optimization, Comput. Methods Appl. Mech. Engrg. 383 (2021) 113918, http://dx.doi.org/10.1016/j.cma.2021.113918, URL https://www.sciencedirect.com/science/article/pii/S0045782521002553.

[43] Z. Huang, G. Lin, A.M. Ardekani, A consistent and conservative volume distribution algorithm and its applications to multiphase flows using Phase-Field models, Int. J. Multiph. Flow. 142 (2021) 103727, http://dx.doi.org/10.1016/j.ijmultiphaseflow.2021.103727, URL https://www.sciencedirect.com/science/article/pii/S0301932221001750.

[44] J. Hötzer, A. Reiter, H. Hierl, P. Steinmetz, M. Selzer, B. Nestler, The parallel multi-physics phase-field framework Pace3D, J. Comput. Sci. 26 (2018) 1–12, http://dx.doi.org/10.1016/j.jocs.2018.02.011, URL https://www.sciencedirect.com/science/article/pii/S1877750317310116.

[45] D. Downing, A. Jones, M. Brandt, M. Leary, Increased efficiency gyroid structures by tailored material distribution, Mater. Des. 197 (2021) 109096, http://dx.doi.org/10.1016/j.matdes.2020.109096, URL https://www.sciencedirect.com/science/article/pii/S0264127520306316.

[46] C.A. Lambert, L.H. Radzilowski, E.L. Thomas, Triply periodic level surfaces as models for cubic tricontinuous block copolymer morphologies, Phil. Trans. R. Soc. A 354 (1715) (1996) 2009–2023, http://dx.doi.org/10.1098/rsta.1996.0089, URL https://www.scopus.com/inward/record.uri?eid=2-s2.0-3042891541&doi=10.1098%2frsta.1996.0089&partnerID=40&md5=c9c330c2d7aa7d22af410c88ba29fbad. Cited by: 48.

[47] I. Maskery, L. Sturm, A. Aremu, A. Panesar, C. Williams, C. Tuck, R. Wildman, I. Ashcroft, R. Hague, Insights into the mechanical properties of several triply periodic minimal surface lattice structures made by polymer additive manufacturing, Polymer 152 (2018) 62–71, http://dx.doi.org/10.1016/j.polymer.2017.11.049, URL https://www.sciencedirect.com/science/article/pii/S0032386117311175. SI: Advanced Polymers for 3DPrinting/Additive Manufacturing.

[48] B. Nestler, A. Choudhury, Phase-field modeling of multi-component systems, Curr. Opin. Solid State Mater. Sci. 15 (3) (2011) 93–105, Applications of Phase Field Modeling in Materials Science and Engineering.

[49] A.A. Wheeler, W.J. Boettinger, G.B. McFadden, Phase-field model for isothermal phase transitions in binary alloys, Phys. Rev. A 45 (10) (1992) 7424.

[50] D. Schneider, F. Schwab, E. Schoof, A. Reiter, C. Herrmann, M. Selzer, T. Böhlke, B. Nestler, On the stress calculation within phase-field approaches: a model for finite deformations, Comput. Mech. 60 (2) (2017) 203–217, http://dx.doi.org/10.1007/s00466-017-1401-8.

[51] S.M. Allen, J.W. Cahn, A microscopic theory for antiphase boundary motion and its application to antiphase domain coarsening, Acta Metall. 27 (6) (1979) 1085–1095, http://dx.doi.org/10.1016/0001-6160(79)90196-2, URL https://www.sciencedirect.com/science/article/pii/0001616079901962.

[52] H. Garcke, B. Nestler, B. Stoth, A MultiPhase field concept: Numerical simulations of moving phase boundaries and multiple junctions, SIAM J. Appl. Math. 60 (1) (1999) 295–315, http://dx.doi.org/10.1137/S0036139998334895.

[53] R. Kienzler, R. Schroeder, Elastizitaetsgesetz, in: Einfuehrung in Die Hoehere Festigkeitslehre, Springer Berlin Heidelberg, Berlin, Heidelberg, 2019, pp. 111–166, http://dx.doi.org/10.1007/978-3-642-24382-0_4.

[54] D. Schneider, O. Tschukin, A. Choudhury, M. Selzer, T. Böhlke, B. Nestler, Phase-field elasticity model based on mechanical jump conditions, Comput. Mech. 55 (5) (2015) 887–901, http://dx.doi.org/10.1007/s00466-015-1141-6.

[55] A.G. Khachaturyan, Theory of Structural Transformations in Solids, John Wiley and Sons, New York, NY, 1983.

[56] M. Selzer, Mechanische und Strömungsmechanische Topologieoptimierung mit der Phasenfeldmethode (Ph.D. thesis), Karlsruhe Institute of Technology, 2014, http://dx.doi.org/10.5445/IR/1000049243.

[57] P. Hoffrogge, A. Mukherjee, E. Nani, P.K. Amos, F. Wang, D. Schneider, B. Nestler, Multiphase-field model for surface diffusion and attachment kinetics in the grand-potential framework, Phys. Rev. E 103 (3) (2021) 033307, http://dx.doi.org/10.1103/PhysRevE.103.033307.

[58] B. Nestler, F. Wendler, M. Selzer, B. Stinner, H. Garcke, Phase-field model for multiphase systems with preserved volume fractions, Phys. Rev. E 78 (2008) 011604, http://dx.doi.org/10.1103/PhysRevE.78.011604, URL https://link.aps.org/doi/10.1103/PhysRevE.78.011604.

[59] A. Prahs, M. Reder, D. Schneider, B. Nestler, Thermomechanically coupled theory in the context of the multiphase-field method, Int. J. Mech. Sci. 257 (2023) 108484, http://dx.doi.org/10.1016/j.ijmecsci.2023.108484, URL https://www.sciencedirect.com/science/article/pii/S0020740323003867.

[60] M. Ahamed, H. Wang, P. Hazell, From biology to biomimicry: Using nature to build better structures – a review, Constr. Build. Mater. 320 (2022) 126195, http://dx.doi.org/10.1016/j.conbuildmat.2021.126195.

[61] A. John, M. John, The foamed structures in numerical testing, AIP Conf. Proc. 1922 (1) (2018) 050003, http://dx.doi.org/10.1063/1.5019057, arXiv:https://aip.scitation.org/doi/pdf/10.1063/1.5019057. URL https://aip.scitation.org/doi/abs/10.1063/1.5019057.

[62] A. John, M. John, Foam metal and honeycomb structures in numerical simulation, Ann. Faculty Eng. Hunedoara 14 (4) (2016) 27.

[63] R. Attarzadeh, M. Rovira, C. Duwig, Design analysis of the "Schwartz D" based heat exchanger: A numerical study, Int. J. Heat Mass Transfer 177 (2021) 121415, http://dx.doi.org/10.1016/j.ijheatmasstransfer.2021.121415, URL https://www.sciencedirect.com/science/article/pii/S0017931021005184.

[64] Z. Chen, Y.M. Xie, X. Wu, Z. Wang, Q. Li, S. Zhou, On hybrid cellular materials based on triply periodic minimal surfaces with extreme mechanical properties, Mater. Des. 183 (2019) 108109, http://dx.doi.org/10.1016/j.matdes.2019.108109, URL https://www.sciencedirect.com/science/article/pii/S0264127519305477.